Supporting Information

Gibbs–Curie–Wulff-Directed 2D Cocrystal Evolution for Tunable In-Plane Anisotropic and Isotropic Photon Transmission

Yong Liu,†,[a] Fang Ding,†,[a] Zhaoyang Guo,[a] Weiguang Zhang,[a] Xu Zhang,[a] Shuo Jiang,[a] Kelin Yang,[a] Yali Cao,[a] Zhenhua Gao,[b] Lei Wang,[c] Ming Ma,*,[a] Xue-Dong Wang,[c] and Wei Zhang*,[a]

[a] Key Laboratory of Chemical Biology and Traditional Chinese Medicine Research (Ministry of Education), and Key Laboratory of Phytochemical R&D of Hunan Province, and Key Laboratory of the Assembly and Application of Organic Functional Molecules of Hunan Province, Institute of Interdisciplinary Studies, College of Chemistry and Chemical Engineering, Hunan Normal University, Changsha 410081, China.

[b] School of Materials Science & Engineering, Qilu University of Technology (Shandong Academy of Sciences), Jinan 250353, China.

[c] Institute of Functional Nano & Soft Materials (FUNSOM), Soochow University, Suzhou 215123, China.

†These authors contributed equally to this work.

*E-mails: mingma@hunnu.edu.cn, wzhang0222@hunnu.edu.cn

Contents

Materials and experimental details

1. Materials

The model compounds used in this work, i.e., 4-(4-Dimethylaminostyryl)quinoline (DMAQ) and 1,4-Diiodotetrafluorobenzene (FDIB) were purchased from Sigma-Aldrich and used without further purification.

2. Preparation of cocrystal microstructures

Three kinds of DMAQ-FDIB cocrystal microstructures were controllably prepared via a liquid phase co-assembly strategy. In a typical fabrication (See Figure S3), a stock (100 μL) freshly mixed solution of DMAQ and FDIB (12:6 mM) in acetonitrile (CH_3CN) was drop-casted onto the glass substrate at different temperature (~40 °C, ~20 °C and ~0 °C) that was placed in a semi-enclosed container (120 mL), and then the slowly evaporating of the solvent would initiate the nucleation and self-assembly of DMAQ-FDIB cocrystals. After the solvent completely evaporated (~30 min for ~40 °C, ~70 min for ~20 °C, and ~180 min for ~0 °C), the cocrystal microstructures were finally obtained. The final crystallization time depends not only on the temperature but also on the size and number of the openings of the container; however, the openings should be kept consistent across different temperatures. It should be noted that, the temperature of nucleation and growth is very critical for the controlled synthesis of cocrystal microstructures, in which the elongated hexagonal microplates were observed at high ambient temperature (~40 °C), while regular hexagonal microplates were obtained at ~20 °C, and the rhomb microplates were achieved at low temperature (~0 °C).

3. Structural characterizations

The morphology and crystallinity of the as-prepared 2D organic cocrystals were examined by scanning electron microscopy (SEM, Hitachi S-4800). Powder X-ray diffraction (PXRD, Japan Rigaku D/max-2500) was measured with Cu Ka radiation.

4. Theoretical calculations

Morphological prediction: The theoretical growth morphologies of DFC cocrystals were calculated by using the Materials Studio software based on the attachment energy theory.[1] The molecular configurations were firstly optimized based on the single-crystal structures using the Build Bonds. The calculations about morphology and energy were performed through Morphology modules of the Material Studio software.

Surface energy calculation: The surface energies for the different crystal planes of DFCs cocrystal were calculated by using the Materials Studio software.[2] The molecular configurations were firstly optimized based on Forcite modules. Then the crystal-plane surface energies were calculated based on equilibrium morphologies.

Binding energy calculation: The optimal relative steric configuration of DMAQ-FDIB and DMAQ-DMAQ complexes were simulated and calculated by using density functional theory (DFT) B3LYP-D3(BJ)/def2-TZVP, BSSE from the Gaussian 09 program.[3] Thermal correction of the DMAQ-FDIB and DMAQ-DMAQ intermolecular binding energy were calculated by the harmonic approximation based on the optimized structures under 298.15 K and 1 atm pressure. The calculated structures were verified to have no imaginary frequency for all structures.

Transition dipole moment calculation: The geometry optimizations of DMAQ-FDIB dimer in DFCs single crystals were performed, respectively, by B3LYP/6-31+G(d,p) from the Gaussian 09 program,[4] where the LanL2DZ basis set was used for the iodine atom. After the optimization, the transition dipole moment of DMAQ-FDIB molecular geometries were calculated by the time-dependent density functional theory TD//B3LYP/6-31+G(d,p).

5. Optical measurements

The fluorescence spectra were measured with Hitachi F-7000 spectrophotometers. Bright-field optical images and fluorescence microscopy images were taken from an inverted fluorescence microscope (Nikon TE2000-U) by exciting the samples with a mercury lamp. The schematic illustration of the experimental setup for single-microplate optical characterization is shown in Figure S8. A single microplate dispersed on a glass substrate (refractive index about 1.5) was excited locally at different position with a 405 nm semiconductor laser vertically focused down to a ~12 μm diameter spot through an objective (Nikon CFLU Plan, 20×, N.A. = 0.5). The excitation laser was filtered with a 405 nm band-pass filter. The pump power at the input was altered by the neutral density filters. The PL signals from the microcrystals were filtered with a 420 nm long-pass emission to eliminate the excitation light, and recorded with a thermal-electrically cooled fiber-optic spectrometer.

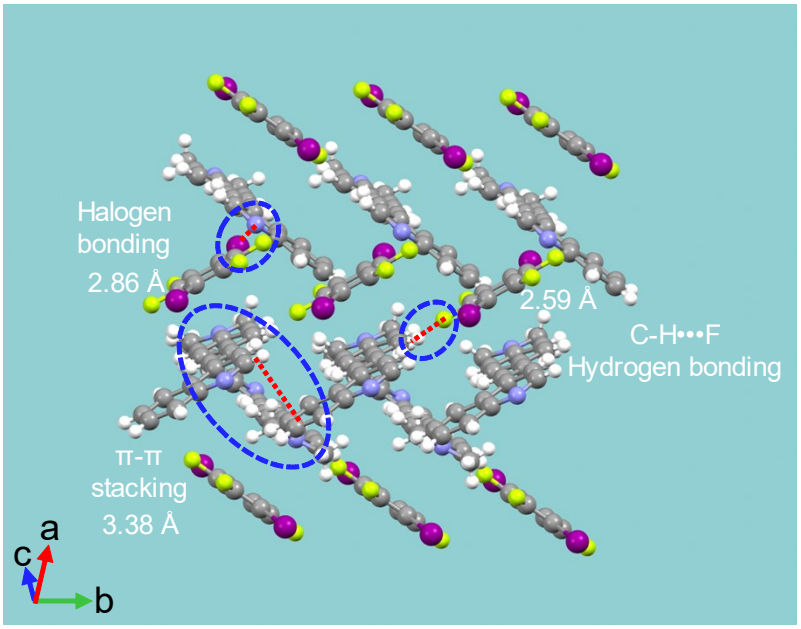

Figure S1. Molecular packing and interactions of DFC cocrystal.

According to the single-crystal data, the DFC cocrystal stacked with a D/A segregated-stacking form, consist of the DMAQ-DMAQ π-π stacking (3.38 Å) along [010], DMAQ-FDIB halogen-bonding (2.86 Å) along [101], and DMAQ-FDIB C-H···F (2.59 Å) interactions, which all collectively drive the aggregation of the DMAQ and FDIB molecules into 2D microcrystals.

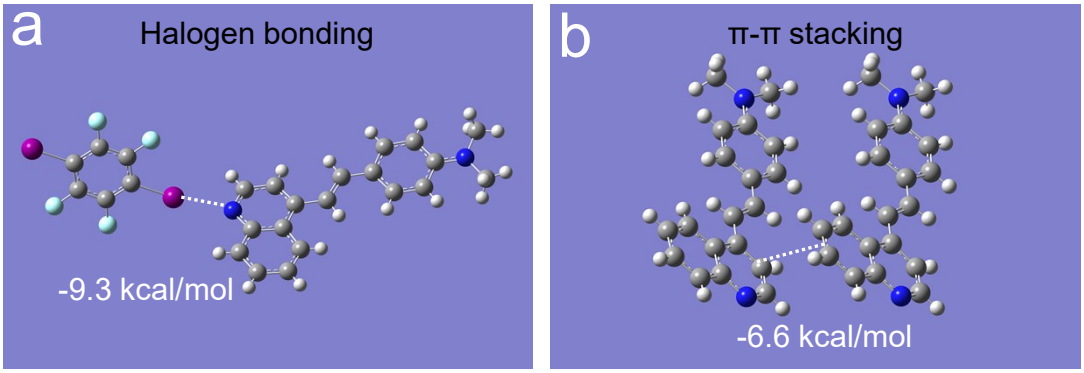

Figure S2. Simulated optimal steric configuration of DMAQ-FDIB complex (a) and DMAQ-DMAQ complex (b) by DFT calculation at B3LYP-D3(BJ)/def2-TZVP, BSSE level.

The calculated binding energies for the DMAQ-FDIB complex and DMAQ-DMAQ complex are -9.3 kcal mol^{-1} and -6.6 kcal mol^{-1}, respectively. which indicates that the π-π stacking interaction is weaker than that of halogen-bonding, showing the possibility to regulate the morphology of 2D cocrystals by changing the external conditions.

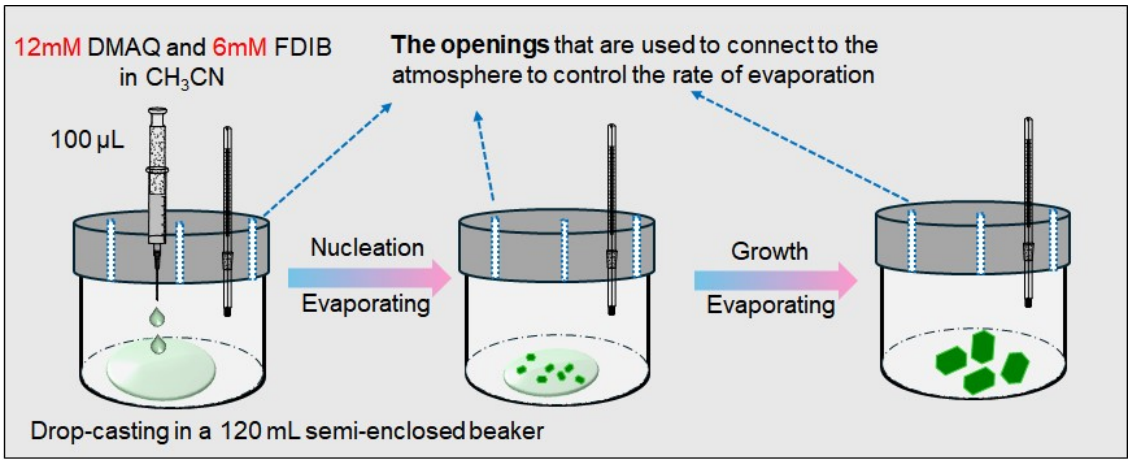

Figure S3. Schematic diagram for the preparation process of the DMAQ-FDIB cocrystals (DFCs) 2D cocrystals.

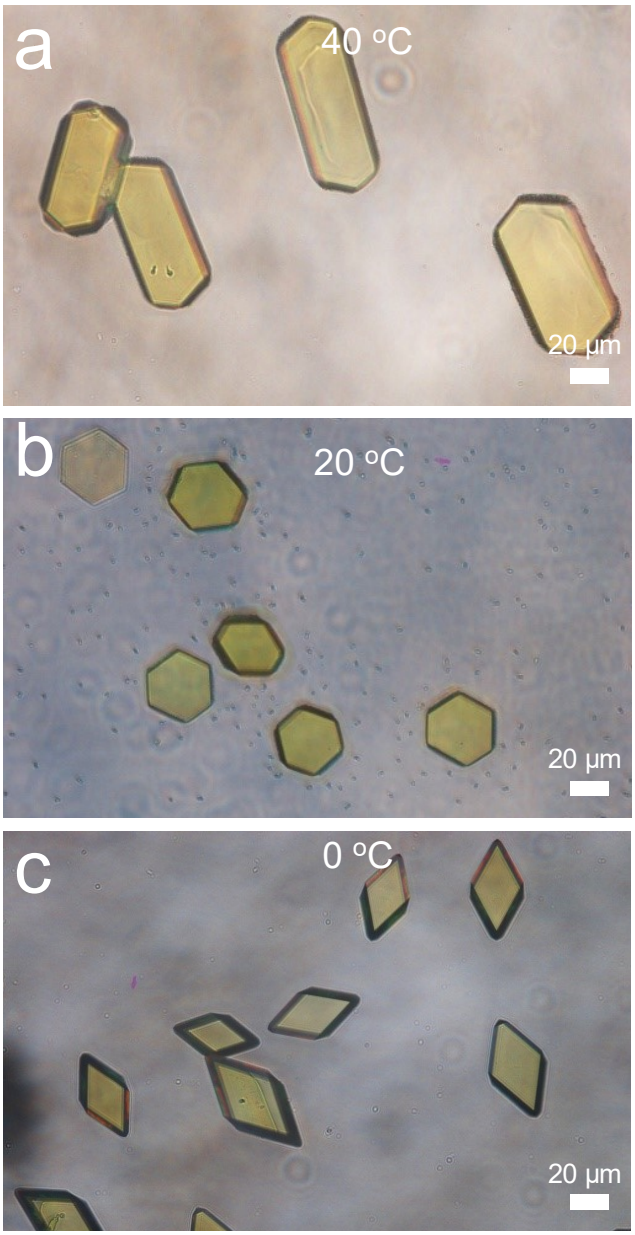

Figure S4. Bright-field images of three kinds of DFC microcrystals with different morphologies grown at different temperatures, which corresponds to Figure 1b-1d.

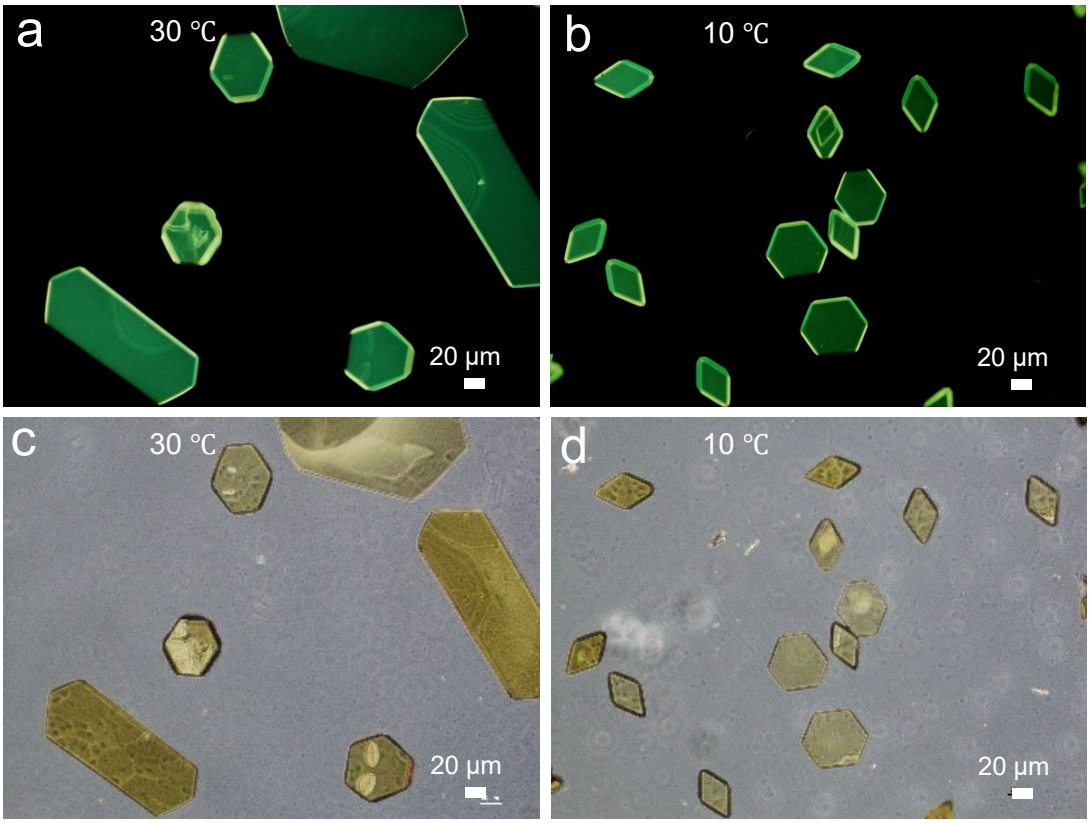

Figure S5. PL and bright-field images of the DFC cocrystals assembled from the temperature of (a, c) 30 °C, and (b, d) 10 °C, respectively.

It can be seen that the temperature is very critical for controlled synthesis of specific cocrystal morphology. When the assembly temperature is ~30 °C, the elongated hexagon and the regular hexagon could be observed simultaneously. Similarly, when the temperature is ~10 °C, the hexagon and rhombus microplates would also be obtained at the same time. Combining with the data of Figure 1b-1d, these results suggest a clear path of 2D morphology evolution from the elongated hexagon to the regular hexagon and then to the rhombus with the changing of temperature.

hkl	d_{hkl}/Å	E_{attach}(kcal mol^{-1})	% Total facet area
{10-1}	13.90	-32.10	44.50
{101}	10.88	-36.29	38.65
{011}	5.91	-95.93	11.10
{110}	5.78	-96.53	5.72

Table S1. Calculated attachment energies of different crystal facets for the DFC cocrystal by using the growth morphology module of Materials Studio package.

The growth morphology algorithm is based on the attachment energy method. It relates the growth rate of a given surface to the potential energy per unit cell gained if a new layer of material attaches to the surface in vacuum. The attachment energy (E_{att}) is defined as the energy released on the addition of a growth slice to the surface of a growing crystal. Thus, the growth rate of the crystal face could be assumed to be proportional to its attachment energy by a layer-by-layer mechanism. In other words, the surfaces with attachment energies smaller in magnitude have lower growth rates and will be morphologically important. For the DFC cocrystal, (10-1) face with lowest attachment energy in magnitude will have smallest growth rates and therefore be more present in the final crystal morphology.

hkl	d_{hkl}/Å	E_{surf}(kcal mol^{-1} Å^{-2})	E_{surf}(mJ m^{-2})
{10-1}	16.21	0.115	79.89
{101}	10.86	0.127	88.22
{011}	5.90	0.133	92.40
{110}	5.80	0.130	90.31

Table S2. Calculated surface free energies of different crystal facets for the DFC cocrystal by using the equilibrium morphology module of Materials Studio package (The E_{surf}(mJ m^2) is converted from E_{surf}(kcal mol^{-1} Å^{-2})).

The equilibrium morphology algorithm is based on the surface free energy method. The surface free energy (E_{surf}) is defined as the needed energy to separate the liquid or solid to coin a new interface in a vacuum. In other words, the energy required to increase the surface area is referred to as the free surface energy. According to the Gibbs-Curie-Wulff theorem, the growth rates of crystal facets are proportional to their surface energies, in which the crystal faces with larger surface energies would have higher growth rates and thus be less present in the final crystal shape, while the crystal faces with smaller surface energies will have lower growth rates and thus dominate the final crystal morphology. For the DFC cocrystal, the surface free energy of (10-1) facet was found to be the lowest compared with other lateral facets and therefore be accessible to obtain 2D microcrystals.

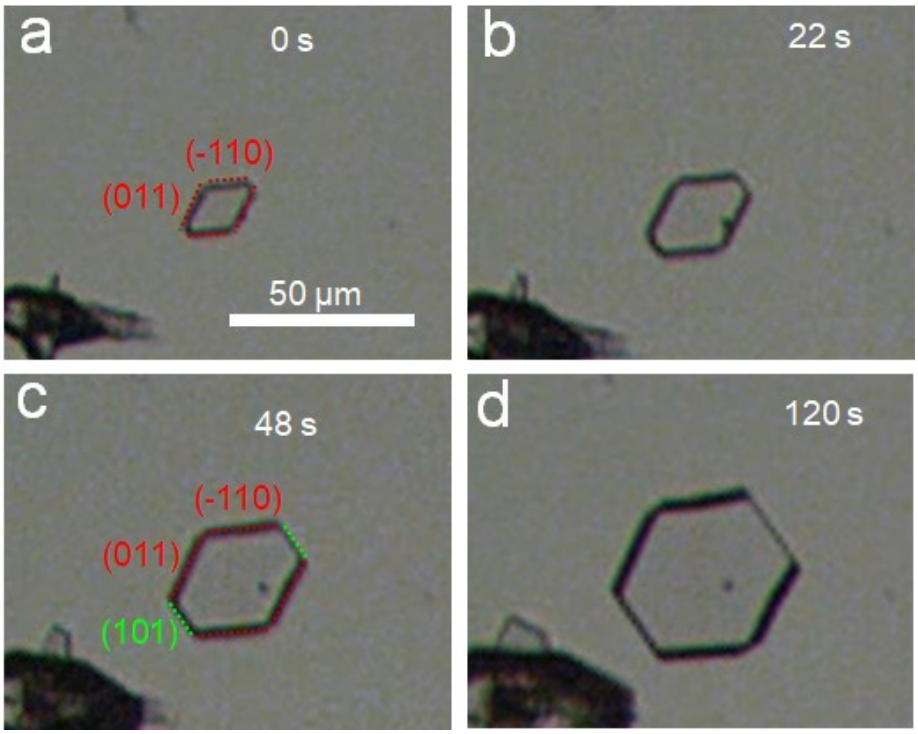

Figure S6. Morphological evolution from a 0°C pre-assembled DFC rhombus microcrystal after heating (10-30 °C), in which, for convenient microscopic observation, an infrared heating lamp was used to rapidly heat a partially assembled rhombus system at 0 °C, and its morphological evolution was subsequently observed.

At 0 °C (Figure S6a), rhombus-shaped microcrystals are predominantly formed due to the higher surface energy of the (101) facet, which results in a faster growth rate and negligible surface exposure than those of the (011) and (-110) facets. However, when a rhombus microcrystal at the initial stage of assembly is suddenly heated to above 10 °C (Figure S6b-d), it continues to grow and gradually evolves into a hexagonal microcrystal, accompanied by the progressive exposure of the originally hidden (101) facets. This behavior indicates that temperature elevation induces markedly different reductions in the surface energies of the (101) and (011)/(-110) facets. In particular, the (101) facet exhibits a much larger decrease in surface energy, changing from being higher than to comparable to or even lower than that of the (011)/(-110) facets, thereby driving the observed morphological transition from a small rhombus to a big hexagonal microcrystal.

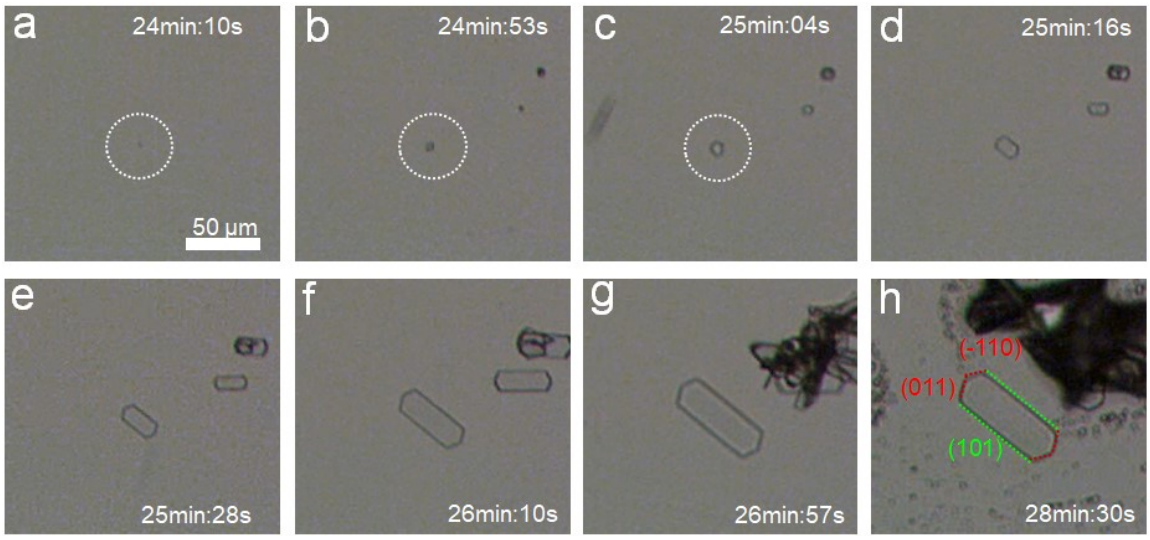

Figure S7. Time-dependent morphological evolution of an individual DFC microcrystal during growth at 40 °C.

We can observe that, at the extremely rapid nucleation stage (Figure S7a), the cocrystals appear as very small spherical particles without pronounced anisotropy. However, upon entering the growth stage (Figure S7b-c), the growth rates of the (011) and (-110) facets are markedly faster than that of the (101) facet, resulting in pronounced anisotropic growth and the eventual formation of elongated hexagonal morphologies (Figure S7d-h). This behavior originates from the fact that, at 40 °C, the surface energies of the (011) and (-110) facets are comparable and exceed that of the (101) facet.

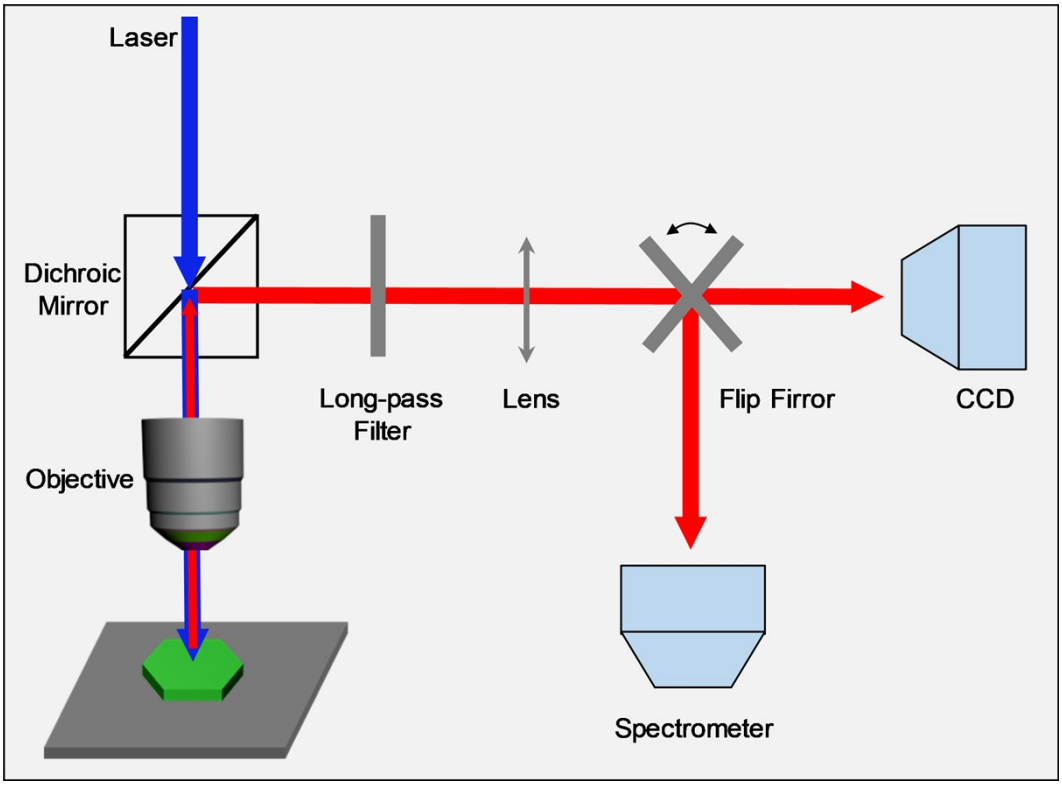

Figure S8. Schematic illustration of the experimental setup for the optical waveguide characterization.

To measure the micro-area waveguiding PL spectra, A single cocrystal microplate dispersed on a glass substrate (refractive index about 1.5) was excited locally at different position with a 405 nm semiconductor laser vertically focused down to a ~12 μm diameter spot through an objective (Nikon CFLU Plan, 20×, N.A. = 0.5). The excitation laser was filtered with a 405 nm band-pass filter. The pump power at the input was altered by the neutral density filters. The PL signals from the microplate were filtered with a 420 nm long-pass emission to eliminate the excitation light, and recorded with a fiber-optic spectrometer.

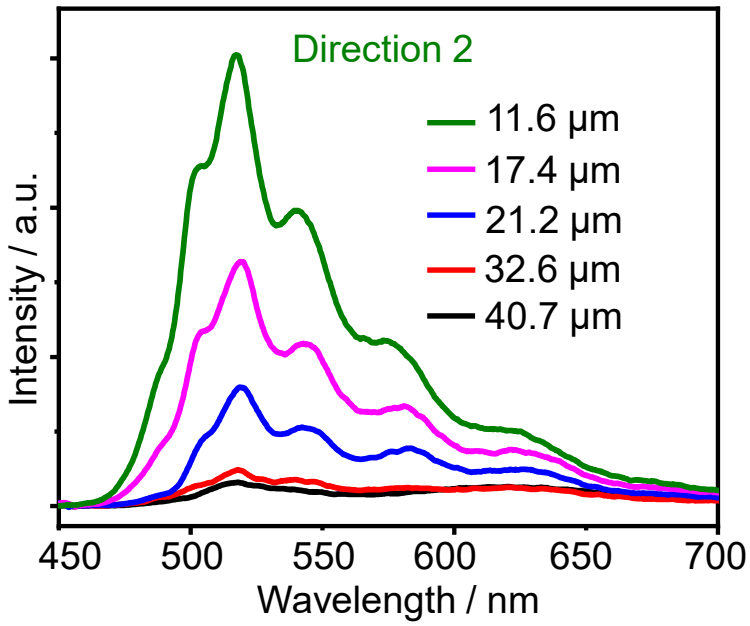

Figure S9. Spatially resolved micro-PL spectra for the D2 edge of a hexagonal microplate shown in Figure 3b, as the waveguide distance increases.

The outcoupled PL signals from the D2 edge in a hexagonal microplate, rapidly decay when changes the excitation spot to increase the waveguiding distances.

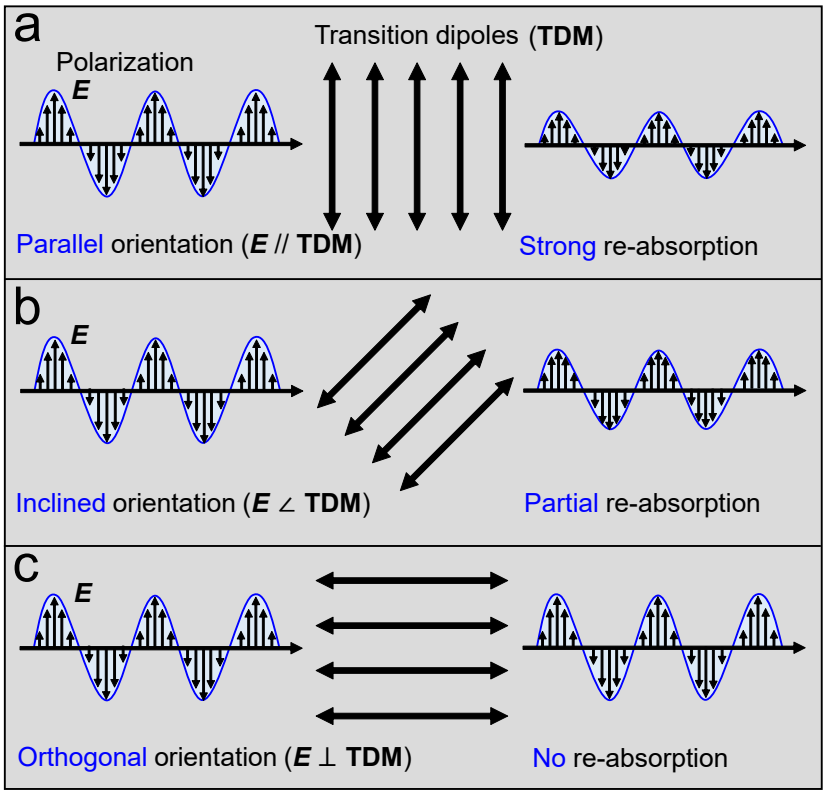

Figure S10. Orientation-controlled photon–dipole interactions leading to different re-absorption waveguide losses.

For active optical waveguides, the self-emissive photons can interact with the molecular dipoles to some extent during transmission, resulting in re-absorption loss, where the magnitude of loss is related to the relative orientation between the polarization of light and the molecular transition dipole moment (TDM). When the TDM is parallel to the polarization of the propagated photons, strong re-absorption occurs. In comparison, if the TDM are perpendicular to the photon polarization, no re-absorption takes place. Furthermore, when the TDM is inclined relative to the polarization of the propagated photons, partial re-absorption happens, which is also the most commonly observed phenomenon in existing studies.

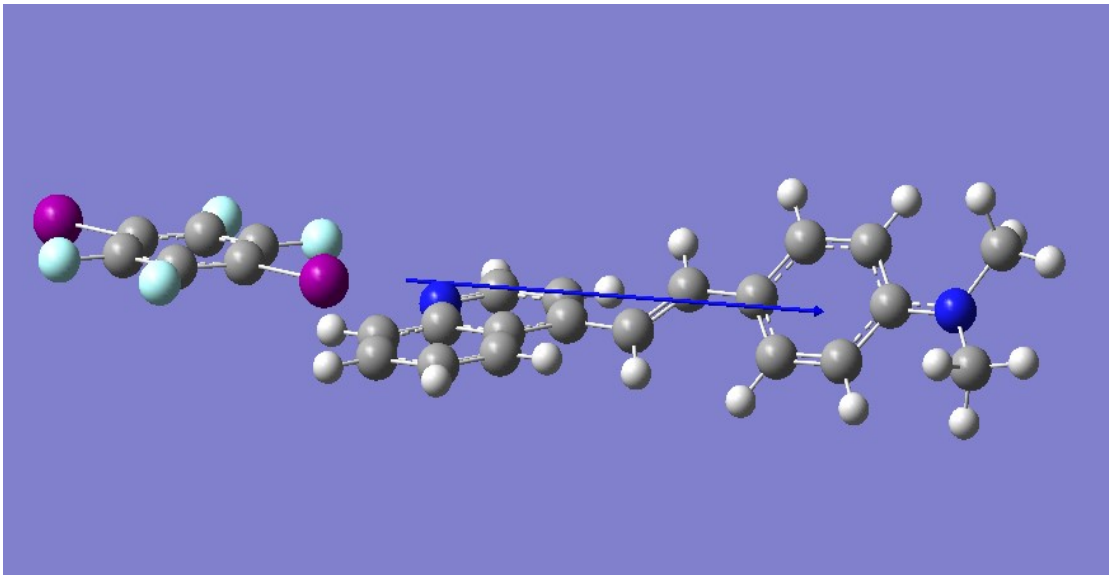

Figure S11. The orientation of the transition dipole moment of a DMAQ-FDIB dimer (blue line with arrow).

The TDDFT calculated result shows that the transition dipole moment is nearly parallel to the molecular long axis of DAMQ in the DFCs. Combining the molecular orientation in the DFCs microplates, the transition dipoles of DFCs were deduced to adopt an approximatively horizontal orientation along the width direction, i.e., [101].

References:

(1) Winn, D.; Doherty, M. F. Modeling Crystal Shapes of Organic Materials Grown from Solution. *AlChE J.* **2000**, *46* (7), 1348-1367.

(2) Zhuo, M. P.; Wu, J. J.; Wang, X. D.; Tao, Y. C.; Yuan, Y.; Liao, L. S. Hierarchical self-assembly of organic heterostructure nanowires. *Nat. Commun.* **2019**, *10* (1), 3839.

(3) Zhao, Y.; Truhlar, D. G. The M06 suite of density functionals for main group thermochemistry, thermochemical kinetics, noncovalent interactions, excited states, and transition elements: two new functionals and systematic testing of four M06-class functionals and 12 other functionals. *Theor. Chem. Acc.* **2008**, *120* (1), 215-241.

(4) Lee, C.; Yang, W.; Parr, R. G. Development of the Colle-Salvetti correlation-energy formula into a functional of the electron density. *Phys. Rev. B* **1988**, *37* (2), 785-789.